RESEARCH ARTICLE
PLANETARY SCIENCES

Earth and Planetary Physics
10: 417–426, 2026
doi: 10.26464/epp2026047

Martian ion currents and escape driven by interplanetary magnetic field orientation based on hybrid simulations

HengLe Du[1,2], BinBin Ni[1*], Xiao-Dong Wang[2*], Shahab Fatemi[3], and Xing Cao[1]

[1]School of Earth and Space Science and Technology, Wuhan University, Wuhan 430074, China;

[2]Solar System Physics and Space Technology Programme, Swedish Institute of Space Physics, SE-981 92 Kiruna, Sweden;

[3]Department of Physics, Umeå University, SE-901 87 Umeå, Sweden

Key Points:

- The transition to a parallel interplanetary magnetic field (IMF) generates mass-dependent cross-flow plumes that extend asymmetrically into the $-Y_{\mathrm{MSE}}$ hemisphere, where MSE is the Mars solar electric coordinate frame.
- The cross-flow plumes act as additional obstacles, governing the surrounding solar wind flow and causing proton currents to diffuse in the $-Y_{\mathrm{MSE}}$ hemisphere.
- Ion escape reaches a maximum under a parallel IMF, driven by a shift from tail-dominated to plume-dominated flow with significant upstream enhancement.

Citation: Du, H. L., Ni, B. B., Wang, X.-D., Fatemi, S., and Cao, X. (2026). Martian ion currents and escape driven by interplanetary magnetic field orientation based on hybrid simulations. *Earth Planet. Phys.*, *10*(3), 417–426. http://doi.org/10.26464/epp2026047

Abstract: As a planet lacking a global magnetic field, Mars interacts directly with the solar wind, forming an induced magnetosphere that mediates energy transfer and atmospheric ion loss. The topology of this interaction and the resulting atmospheric ion escape are strongly influenced by the orientation of the interplanetary magnetic field (IMF). In this study, we utilize a hybrid model to investigate how variations in the IMF orientation shape ion current systems and atmospheric ion escape rates of O^+, O_2^+, CO_2^+. We first perform simulations with a constant $|B_{\mathrm{sw}}|$, where varying the IMF cone angle results in different strengths of the convective electric field ($E_{\mathrm{sw}} = V_{\mathrm{sw}} \times B_{\mathrm{sw}}$). Our results suggest that the spatial morphology of ion plumes undergoes a substantial evolution, forming a distinct cross-flow plume as the IMF rotates from perpendicular to parallel. These ion plumes exhibit a mass-dependent deflection, where heavier CO_2^+ travel farther with larger gyroradii than lighter O^+, acting as an asymmetric obstacle in the $-Y_{\mathrm{MSE}}$ hemisphere (where MSE is the Mars solar electric coordinate frame). In turn, the solar wind proton current develops pronounced asymmetries under a parallel IMF, becoming largely diffused in the $-Y_{\mathrm{MSE}}$ hemisphere because of the interaction with the additional plume obstacles. Consequently, the ion escape rates exhibit a nonmonotonic dependence on the IMF orientation, peaking under a parallel IMF as escape shifts from a tail- to plume-dominated flow with substantial upstream enhancement. To decouple the effects of IMF geometry from those of the convective electric field, we further conduct a comparative simulation with constant B_y (hence constant $|E_{\mathrm{sw}}|$), where the cone angle is varied by changing the B_x component while allowing $|B_{\mathrm{sw}}|$ to vary. With increasing B_x toward a parallel orientation, the total field magnitude grows, causing the Alfvén Mach number (M_A) to decrease from super-Alfvénic to trans-Alfvénic and ultimately to sub-Alfvénic values. Within the range from perpendicular to a 30° cone angle, where the system remains in the super-Alfvénic regime, ion escape is largely insensitive to the growing B_x component. This finding indicates that the magnetic barrier maintains its shielding efficiency under the super-Alfvénic regime.

Keywords: Martian space; ion current; ion escape; interplanetary magnetic field orientation

---

1. Introduction

The interaction between the solar wind and Mars is a pivotal process driving the long-term evolution of the Martian atmosphere. Unlike Earth, which is shielded by a strong intrinsic magnetic field, Mars interacts directly with the solar wind via its conductive ionosphere and localized crustal fields (Acuña et al., 1998; Connerney et al., 1999; Brain et al., 2010; Lundin et al., 2011; Cui J et al., 2018; Li SB et al., 2020; Li XZ et al., 2020). This interaction creates an induced magnetosphere that serves as the primary interface for energy and momentum transfer (Lundin et al., 2008; Jakosky et al., 2015). This environment is sustained by complex current systems that define the magnetospheric boundaries and dictate the spatial distribution of electromagnetic fields. These fields exert forces necessary to accelerate planetary ions (Li SB et al., 2023; Wang XD et al., 2023). Thus, the structure of the current

---

First author: H. L. Du, duhengle@whu.edu.cn
Correspondence to: B. B. Ni, bbni@whu.edu.cn
X.-D. Wang, wang@irf.se
Received 13 FEB 2026; Accepted 30 MAR 2026.

systems effectively determines the pathways and efficiency of ion removal.

The global magnetic topology is inherently linked to the net current density (J_{net}), a relationship that is fundamental to characterizing the magnetospheric structure, energy transport, and resulting ion escape processes (Le G et al., 2004; Ganushkina et al., 2018; Du HL et al., 2022; Shi Z et al., 2022; Wang XD et al., 2023; Zhang C et al., 2025). Ramstad et al. (2020) identified the global current systems within the Martian induced magnetosphere and proposed their qualitative link to energy transfer and planetary ion loss. However, whereas J_{net} defines the overall magnetic structure, understanding the specific dynamics of ion escape requires a kinetic perspective. From a kinetic standpoint, the movement of a specific ion species s can be quantified by its species-specific current density, defined as $J_s = qn_sv_s$, where q is the ion charge, n_s is the number density, and v_s is the bulk velocity. When all ions are singly charged (as is the case in the present study), J_s is directly proportional to the ion flux and thus acts as a precise proxy for ion outflow (Wang XD et al., 2024). This relationship is particularly significant for heavy ions (O^+, O_2^+, and CO_2^+), which are considered tracers for the historical loss of water and provide critical clues regarding the planet's past habitability (Jakosky and Phillips, 2001; Barabash et al., 2007; Brain et al., 2016).

The global morphology of the Martian plasma environment is primarily governed by the interplanetary magnetic field (IMF) orientation (Phillips et al., 1986; Brain et al., 2006; Fang XH et al., 2018; Garnier et al., 2022) and the associated convective electric field (E_{sw}). The IMF cone angle—the angle between the IMF vector and the solar wind velocity—determines the strength of the convective electric field and, in turn, the structure of the induced magnetosphere. As the IMF rotates from a perpendicular toward a quasi-parallel (flow-aligned) configuration, it transitions into a highly degenerate induced magnetosphere: boundaries become less distinct and the system grows more permeable to the solar wind (Du J et al., 2009; Zhang TL et al., 2009; Chang Q et al., 2020; Fowler et al., 2022; Zhang Q et al., 2024, 2025). This erosion of the protective magnetic topology enhances atmospheric ion escape. Crucially, this degenerate induced magnetosphere not only modulates the total escape rate but also reshapes the spatial distribution of escaping ions and alters the balance between major escape channels, such as the ion plume and the magnetotail (Liu K et al., 2009; Zhang Q et al., 2023; Song YH et al., 2025). These structural transitions are accompanied by large-scale rearrangements of the global ion current system. However, a systematic, species-resolved comparison of ion current distributions across IMF cone angles remains largely unexplored.

In this study, we employ three-dimensional (3D) hybrid simulations to investigate the evolution of current density distributions for both heavy ions (O^+, O_2^+, and CO_2^+) and solar wind protons (H^+) as the IMF transitions from a perpendicular to a parallel configuration. We examine how the degenerate induced magnetosphere under low cone angles influences the current structures, and we quantitatively assess the resulting escape rates for O^+, O_2^+, and CO_2^+. This article is organized as follows: Section 2 describes the hybrid model and numerical setup. Section 3 analyzes the simulation results and the IMF dependence of ion currents and escape rates, Section 4 provides a discussion, and Section 5 presents conclusions.

2. Methods

2.1 Theory

Hybrid models provide an effective framework for describing plasma phenomena at ion kinetic scales. In this study, we utilize the Amitis code, a hybrid plasma model implemented on graphics processing units (GPUs) to investigate plasma dynamics (Fatemi et al., 2017). The hybrid approach integrates kinetic and fluid descriptions, where positively charged ions are modeled as kinetic particles, whereas electrons are treated as a massless charge-neutralizing fluid. The evolution of ion motion is governed by the Lorentz force, with their trajectories computed by solving the following equations of motion:

$$\frac{\mathrm{d}\boldsymbol{r}}{\mathrm{d}t} = \boldsymbol{v},\ \frac{\mathrm{d}\boldsymbol{v}}{\mathrm{d}t} = \frac{q}{m}(\boldsymbol{E} + \boldsymbol{v} \times \boldsymbol{B}), \tag{1}$$

where q and m are the ion charge and mass, respectively; $\boldsymbol{r}$ and $\boldsymbol{v}$ are the position and velocity vectors. The terms $\boldsymbol{E}$ and $\boldsymbol{B}$ correspond to the electric and magnetic fields. The electric field $\boldsymbol{E}$ can be decomposed into three nondissipative terms—the convective, Hall, and ambipolar fields—and one dissipative term—the Ohmic field—as formulated by the generalized Ohm's law:

$$\boldsymbol{E} = \overbrace{-\boldsymbol{J}_i \times \boldsymbol{B}/\rho_i}^{\text{convective term}} + \overbrace{\boldsymbol{J}_{\mathrm{net}} \times \boldsymbol{B}/\rho_i}^{\text{Hall term}} - \overbrace{\nabla p_e/\rho_i}^{\text{ambipolar term}} + \overbrace{\eta \boldsymbol{J}_{\mathrm{net}}}^{\text{Ohmic term}}, \tag{2}$$

where $\boldsymbol{J}_i$ is the total ion current ($\boldsymbol{J}_i = \boldsymbol{J}_{\mathrm{H}^+} + \boldsymbol{J}_{\mathrm{O}^+} + \boldsymbol{J}_{\mathrm{O}_2^+} + \boldsymbol{J}_{\mathrm{CO}_2^+}$), $\boldsymbol{J}_{\mathrm{net}} = \nabla \times \boldsymbol{B}/\mu_0$ is the net current density derived from Ampère's law under the radiation-free (Darwin) limit, ρ_i is the ion charge density, p_e is the scalar electron pressure, and η represents the plasma resistivity. Here, the convective (motional) field arises from plasma motion across the magnetic field, whereas the Hall field is driven by cross-field currents. Because both terms are of an inductive nature, they are dependent on the reference frame. The ambipolar term, in contrast, originates from the charge separation attributable to differential diffusions of electrons and ions, making it independent of the reference frame. The Ohmic term introduces resistivity that can help mitigate numerical instabilities.

2.2 Model Setup

We utilize the MSE coordinate frame, with the x-axis pointing sunward, the z-axis parallel to the solar wind convective electric field (E_{sw}), and the y-axis completing the right-handed system. The 3D computational domain extends ±3 R_{M} along the x-axis and ±6.5 R_{M} along both the y- and z-axes, where R_{M} = 3400 km denotes the Martian radius.

The plasma environment is initialized with a solar wind consisting solely of protons, characterized by a density of 4.9 cm^{-3}, a velocity of 350 km/s along the x-axis, and a proton temperature of 5.9×10^4 K, consistent with the parameters used in Wang XD et al. (2023). Heavy ion species (O^+, O_2^+, and CO_2^+) are injected from the Martian ionosphere, with their net production rates computed using an empirical model (Wang XD et al., 2023). To account for the exobase while excluding the collisional lower atmosphere, an inner spherical boundary is established at a radius of 3600 km, corresponding to the exobase (≈200 km altitude). Any ions intersecting this inner boundary are subsequently removed from the simulation.

To systematically examine how the IMF orientation influences ion currents, we perform four numerical experiments. In all cases, the IMF magnitude is fixed at ~5.6 nT while the cone angle—the angle between the solar wind velocity and the IMF vector—is varied. As detailed in Table 1, the configurations include (i) a perpendicular orientation with a 90° cone angle ([0, 5.59, 0] nT); (ii) a Parker spiral ([−3.13, 4.64, 0] nT); (iii) a cone angle of 30° ([−4.84, 2.80, 0] nT); (iv) a cone angle of 10° (IMF = [−5.51, 0.97, 0] nT); and (v) a quasi-parallel orientation with a 4° cone angle ([−5.58, 0.39, 0] nT). Notably, the 4° cone angle for the parallel orientation is chosen to remain consistent with recent MAVEN (Mars Atmosphere and Volatile EvolutioN) observational constraints (Zhang Q et al., 2024).

2.3 Escape Boundary Setup

To investigate the dependence of escape morphology on upstream IMF orientations, we characterize three primary escape channels: tailward, plume (Dong Y et al., 2015, 2017), and upstream escape (Zhang Q et al., 2024). These channels are defined using a geometric bounding box centered at Mars, following the methodology described by Zhang Q et al. (2024). The dimensions of this box are set at $X_{\mathrm{MSE}} = \pm 1.6\ R_{\mathrm{M}}$ and Y_{MSE}, $Z_{\mathrm{MSE}} = \pm 1.7\ R_{\mathrm{M}}$. Specifically, the ion outflow crossing the $-X_{\mathrm{MSE}}$ boundary at $X = -1.6\ R_{\mathrm{M}}$ is categorized as tail escape, whereas the portion exiting through the $+X_{\mathrm{MSE}}$ boundary at $X = +1.6\ R_{\mathrm{M}}$ represents upstream escape. The combined flux integrated through the lateral boundaries ($\pm 1.7\ Y_{\mathrm{MSE}}$ and $\pm 1.7\ Z_{\mathrm{MSE}}$) is classified as plume escape.

Table 1. Solar wind parameters used in the simulations.

Parameter	Value
IMF in perpendicular case (nT)	[0, 5.59, 0]
IMF in Parker spiral case (nT)	[−3.13, 4.64, 0]
IMF in cone angle 30° case (nT)	[−4.84, 2.80, 0]
IMF in cone angle 10° case (nT)	[−5.51, 0.97, 0]
IMF in parallel case (nT)	[−5.58, 0.39, 0]
Solar wind species	Proton
Density (cm^{-3})	4.9
Velocity (km/s)	350
Ion temperature (K)	5.9×10^4
Electron temperature (K)	3×10^5
Spatial resolution	125 km, ~1.2 proton inertial length
Particles per cell	~20

3. Simulation Results

3.1 Ion and Proton Currents under Various IMF Orientations

To characterize the spatial structure of the induced magnetosphere and its dependence on the upstream magnetic field orientation, we begin by analyzing the current density distributions of O^+, O_2^+, and CO_2^+. Figure 1 presents the current densities of these ion species in the Y_{MSE}–Z_{MSE} plane at $X_{\mathrm{MSE}} = 0\ R_{\mathrm{M}}$, comparing four IMF orientations: perpendicular (Figure 1, panels a1–a3), cone angle 30° (Figure 1, panels b1–b3), cone angle 10° (Figure 1, panels c1–c3), and parallel (Figure 1, panels d1–d3). Because the ion distributions under the Parker spiral IMF configuration do not differ significantly from the perpendicular case, they are not shown here for simplicity. For comparison, Wang XD et al. (2024) presented the ion current distributions in the X_{MSE}–Y_{MSE} and X_{MSE}–Z_{MSE} planes under the perpendicular IMF condition, illustrating the ion plume features, but did not systematically investigate the effects of different IMF cone angles. In these plots, the rows correspond to the three ion species, and the white arrows represent the in-plane ion flux vectors.

Under perpendicular IMF conditions (Figure 1, panels a1–a3), the three heavy ion species exhibit similar morphological features, clustering primarily near the ionosphere. Among them, the current density of O_2^+ ($|J_{O_2^+}|$) is the highest, followed by O^+ and CO_2^+, mainly because of the production rate differences. A well-defined plume structure extends from the ionosphere into the $+Z_{\mathrm{MSE}}$ hemisphere within the $Y_{\mathrm{MSE}} = 0$ plane, providing clear evidence of plume ion escape. As the IMF rotates toward a parallel orientation, a progressive transformation in this morphology becomes evident. In the case of the IMF at a 30° cone angle (Figure 1, panels b1–b3), although the global structure resembles the perpendicular case, an asymmetry stands out, characterized by a slight deflection of the plume toward the $-Y_{\mathrm{MSE}}$ direction.

When the IMF is at a 10° cone angle (Figure 1, panels c1–c3), the plume deflection toward $-Y_{\mathrm{MSE}}$ becomes more pronounced. Crucially, the plume ions now gyrate in a plane almost perpendicular to the solar wind velocity direction because the IMF is almost parallel to the solar wind flow. This so-called cross-flow plume extends beyond the model bow shock distance in the $-Y_{\mathrm{MSE}}$ hemisphere. This cross-flow plume is significantly enhanced under the parallel IMF configuration (Figure 1, panels d1–d3). Unlike the flow-aligned plumes in perpendicular cases, the ions form a cycloidal cross-flow plume structure that extends beyond the nominal shock boundary, notably occupying the $-Y_{\mathrm{MSE}}$ hemisphere. Furthermore, the ion gyroradius increases with increasing ion mass, causing mass-dependent extension of the cross-flow plumes. Using typical upstream solar wind conditions from our simulation inputs ($v = 350$ km/s, $|B_{\mathrm{sw}}| = 5.59$ nT), we estimate the gyroradii of the three dominant heavy ion species. For singly charged ions, the gyroradius scales linearly with mass, yielding approximately 3 R_{M} for O^+, 6 R_{M} for O_2^+, and 8.4 R_{M} for CO_2^+. Notably, the estimated gyroradius of O_2^+ is approximately twice that of O^+, consistent with the mass-dependent extension in Figure 1 (panels d1 and d2). Given that plume plasma velocities are generally lower than that of the upstream solar wind and local magnetic fields may be stronger, the actual gyroradii inside the plumes are expected to be somewhat smaller yet remain on the same order of magnitude.

We further analyze the solar wind proton current systems in the

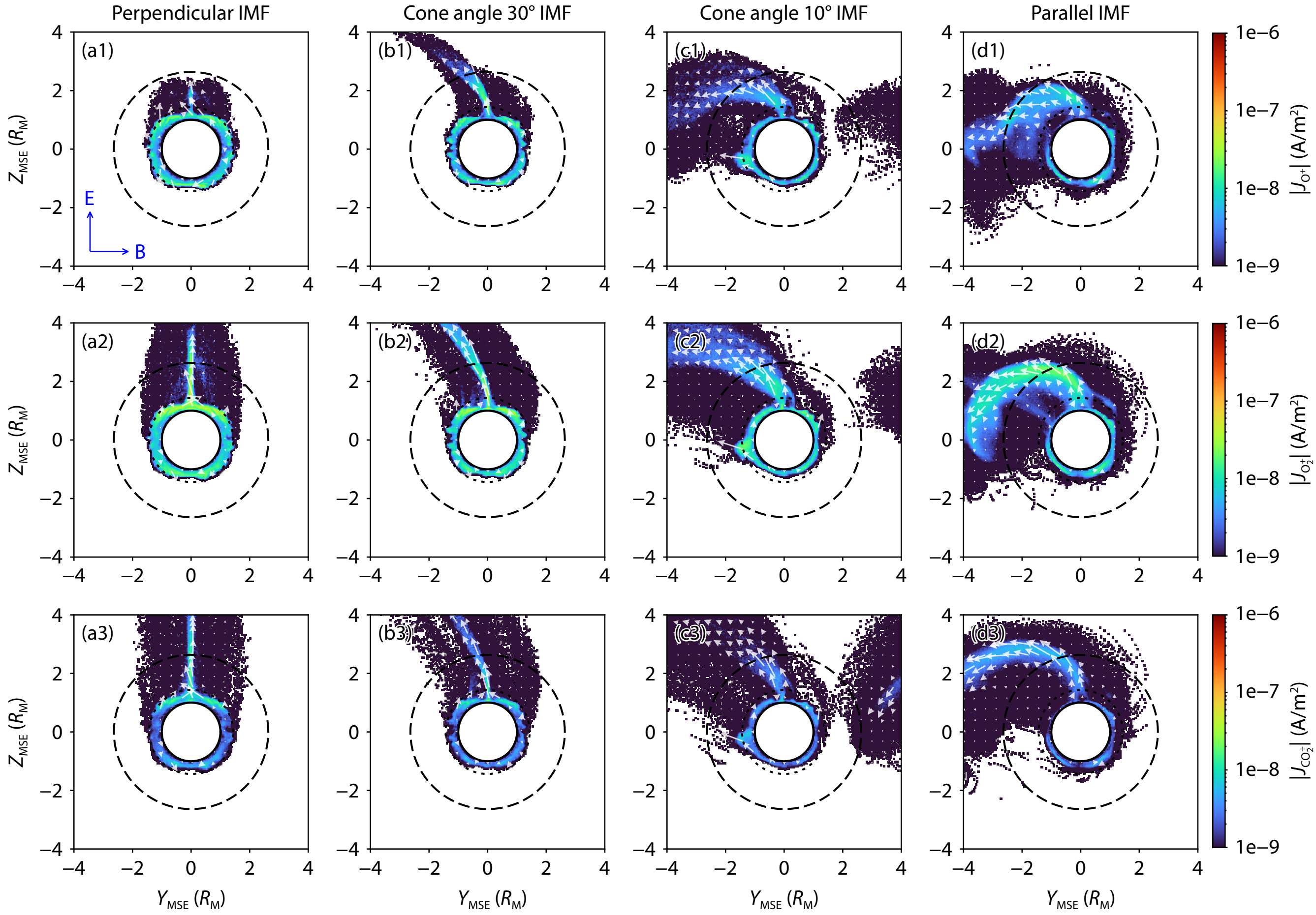

Figure 1. Cross-sectional distributions of ion current density (A/m²) for O^+, O_2^+, and CO_2^+ in the Y_{MSE}–Z_{MSE} plane at $X_{\mathrm{MSE}} = 0\ R_{\mathrm{M}}$ under four IMF orientations: (a1–a3) perpendicular; (b1–b3) cone angle 30°; (c1–c3) cone angle 10°; (d1–d3) parallel. For each IMF condition, the panels from top to bottom show the currents of O^+, O_2^+, and CO_2^+, respectively. The white arrows represent the local direction of the ion flux vectors in the Y_{MSE}–Z_{MSE} plane. The black dashed and dotted lines mark the empirical bow shock and induced magnetosphere boundary (IMB), respectively, from Trotignon et al. (2006).

Y_{MSE}–Z_{MSE} plane. Figure 2 presents slice maps of the solar wind proton current at the terminator ($X_{\mathrm{MSE}} = 0\ R_{\mathrm{M}}$) under four distinct IMF conditions: perpendicular IMF (Figure 2, panels a1–a4), cone angle 30° IMF (Figure 2, panels b1–b4), cone angle 10° IMF (Figure 2, panels c1–c4), and parallel IMF (Figure 2, panels d1–d4). The rows, from top to bottom, display the proton current density, followed by the J_X, J_Y, J_Z components, respectively.

Under the perpendicular IMF condition (Figure 2, panels a1–a4), the solar wind proton flow is symmetrically deflected upon reaching the Martian upstream region. The flow diverges symmetrically, with currents equally deflected in the $\pm Y_{\mathrm{MSE}}$ and $\pm Z_{\mathrm{MSE}}$ directions except for the ion plume region in the central $+Z_{\mathrm{MSE}}$ hemisphere (Figure 2, panel a4). Specifically, within the plume, the proton flow is directed toward the $-Z_{\mathrm{MSE}}$ direction (Figure 2, panel a4). This motion is strictly opposite that of the heavy ions in the corresponding plume region, which travel in the $+Z_{\mathrm{MSE}}$ direction (Figure 1, panels a1–a3). This behavior is attributed to the conservation of momentum between the solar wind protons and the planetary heavy ion plume. As the heavy ions are accelerated in the $+Z_{\mathrm{MSE}}$ direction, momentum conservation dictates that a corresponding “recoil” effect is imparted on the solar wind protons, directly leading to their observed flow toward the $-Z_{\mathrm{MSE}}$ direction. Under the perpendicular IMF configuration, the bow shock is well defined and separates the undisturbed and shocked solar wind. The induced magnetosphere boundary (IMB) appears as the boundary of the drastically dropping proton flux in the simulation (Figure 2, panel a1) and effectively shields the planet from the incident solar wind. The positions of the bow shock and the IMB show good agreement with the empirical model of Trotignon et al. (2006).

As the IMF rotates toward a more field-aligned configuration, a progressive evolution in the current morphology becomes evident. For illustration, we focus here on the case of the cone angle 30° IMF (Figure 2, panels b1–b4) because it exemplifies this transition while retaining close morphological similarity to the perpendicular case. Overall, the deflection state represented by the proton current components remains broadly comparable to the perpendicular IMF case. However, significant asymmetries emerge. In the $-Y_{\mathrm{MSE}}$ hemisphere, where the IMF is parallel to the original bow shock normal, the bow shock altitude decreases

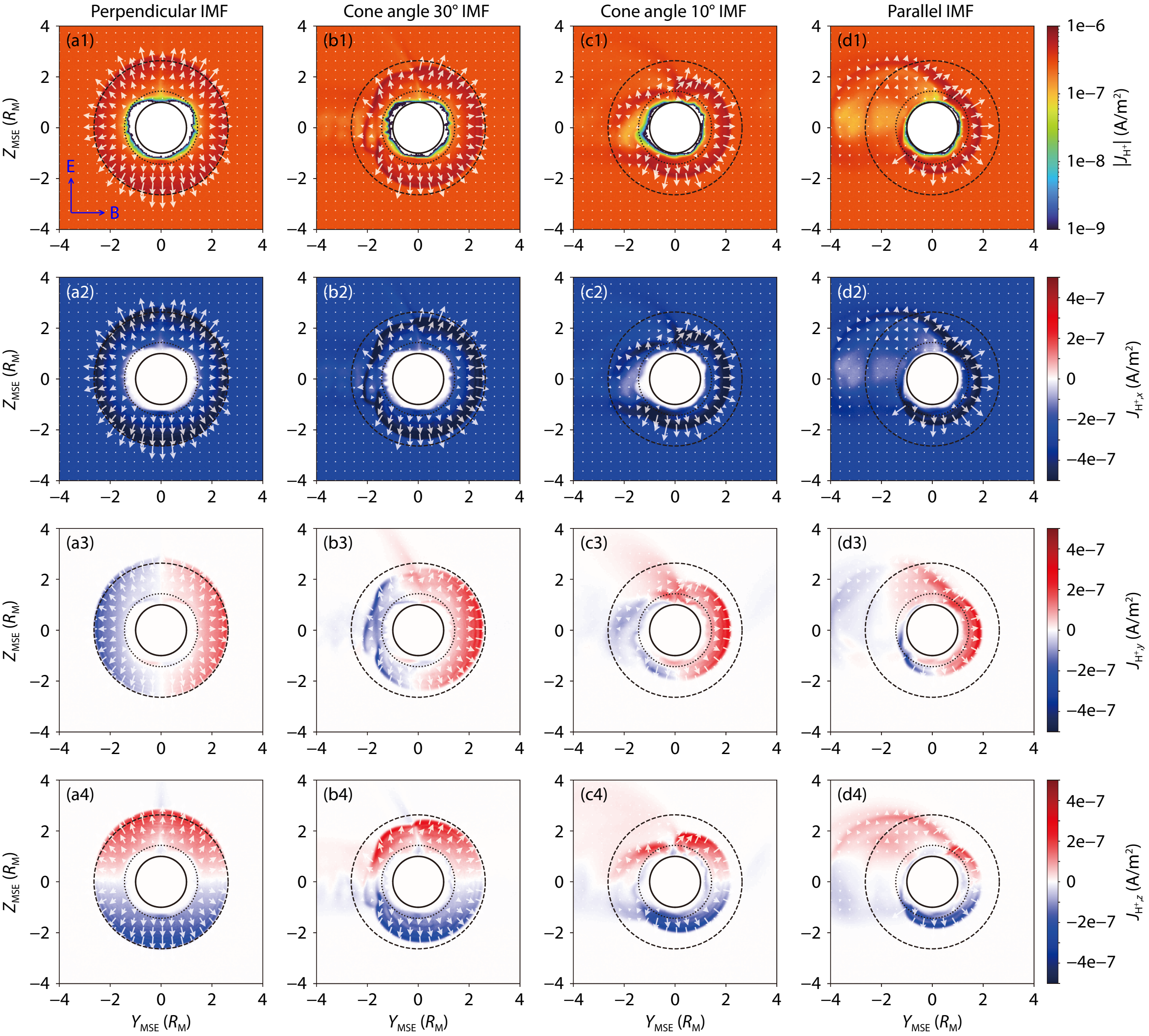

Figure 2. Cross-sectional maps of proton current density (A/m^2) in the Y_{MSE}–Z_{MSE} plane at X_{MSE} = 0 R_M under four IMF orientations. From left to right, the columns correspond to: (a1–d1) perpendicular IMF; (a2–d2) cone angle 30° IMF; (a3–d3) cone angle 10° IMF; (a4–d4) parallel IMF. Each row presents, from top to bottom, the proton current density, J_X, J_Y, and J_Z components, respectively. The white arrows denote the local direction of the proton flux vectors, and the black dashed (bow shock) and dotted (IMB) curves correspond to the empirical boundaries defined by Trotignon et al. (2006).

significantly and exhibits marked disturbances, consistent with the nominal characteristics of the quasi-parallel shock (Burgess et al., 2005). The standoff distance in the +Y_{MSE} hemisphere, where the IMF is perpendicular to the bow shock normal, remains roughly unchanged and stable. Notably, within the plume region, the proton flow is deflected toward the +Y_{MSE} and −Z_{MSE} directions. This flow pattern is consistent with the recoil effect resulting from the heavy ion plume under the 30° cone angle configuration (Figure 1, panels b1–b3). Furthermore, the IMB shows a general decrease in altitude and enhanced fluctuations on the −Y_{MSE} side compared with the perpendicular IMF case (Figure 1, panels b1).

The asymmetry between ±Y_{MSE} hemispheres, or the quasi-perpendicular and the quasi-parallel sides of the bow shock, becomes more pronounced as the cone angle decreases further. Under the cone angle 10° IMF condition (Figure 2, panels c1–c4), the proton current distribution in the +Y_{MSE} hemisphere retains a consistent structure. The bow shock still develops well while being located even closer to Mars than in the 30° cone angle case. In the −Y_{MSE} hemisphere, however, the proton current not only weakens significantly but also exhibits a fragmented distribution, indicating substantial erosion of the quasi-parallel bow shock.

Under the parallel IMF condition (Figure 2, panels d1–d4), the asymmetry reaches its peak. In the +Y_{MSE} hemisphere, the current maintains a coherent structure, revealing that the bow shock persists—although its position is much closer to the planet. In contrast, the current distribution in the $-Y_{\mathrm{MSE}}$ hemisphere undergoes a marked breakdown. Specifically, in the $-Y_{\mathrm{MSE}}/-Z_{\mathrm{MSE}}$ quadrant near Mars, the presence of distinct $-J_y$ and $-J_z$ components indicates that typical proton deflection still occurs, yet the shock boundary shifts inward to the nominal IMB position. Furthermore, weaker and irregularly distributed $\pm J_y$ and $\pm J_z$ components are observed extending well beyond the empirical bow shock in the $-Y_{\mathrm{MSE}}$ hemisphere. This irregularity is attributed to the formation of a heavy ion cross-flow plume structure directed toward $-Y_{\mathrm{MSE}}$. Consequently, driven by the parallel IMF geometry, the previously continuous shock structure loses its coherence and effectively disappears in this region.

In general, the current distribution analysis of heavy ions and solar wind protons reveals that parallel IMF conditions significantly influence the current and plasma structure in Martian space. Specifically, with the IMF rotating from perpendicular to parallel, the convective electric field progressively decreases, resulting in a shrinking of the bow shock and IMB. Furthermore, the parallel IMF facilitates the formation of the cross-flow plume, which extends beyond the nominal bow shock boundary in the $-Y_{\mathrm{MSE}}$ hemisphere. The gyroradii of different ion species depend on their mass-to-charge ratios. The cross-flow plume functions as an expansion of the ionospheric obstacle to the solar wind, governing the solar wind flow pattern around it. As a result, solar wind protons are deflected in the $\pm Y_{\mathrm{MSE}}$ and $\pm Z_{\mathrm{MSE}}$ directions around the plume–ionosphere obstacle. Because the cross-flow plume extends beyond the empirical bow shock position, the macroscopic coherence of the bow shock disappears in this region.

To quantitatively assess how the cross-flow plume influences the solar wind flow, we analyze the energy transfer rate to solar wind protons and heavy ions (O^+, O_2^+, and CO_2^+; Supplementary Figure S1) (Wang XD et al., 2024). The energy transfer rate to each ion species is calculated as $\boldsymbol{E}\cdot\boldsymbol{J}_i$, where $\boldsymbol{E}$ is the electric field vector and $\boldsymbol{J}_i$ is the current density vector of the ion species i. For solar wind protons (Figure S1, panels a1–d1), the disturbances and energy transfer in the interaction with Mars are caused by two obstacles: the induced magnetosphere and the planetary ion plume. As exemplified in Figure S1 (panels a1 and a2), the induced magnetosphere causes the bow shock to slow the solar wind (green circle at r = ~2.5 R_{M}) and allow the relaxation of the shocked solar wind in the terminator plane (magenta area between the bow shock and the IMB). The planetary ion plume (Figure S1, panels a2–d2) gains energy directly from the solar wind interaction because of the motional electric field, so the region of the solar wind losing energy overlaps with the planetary ion plume gaining energy.

As the IMF cone angle decreases, the influences of both obstacles vary accordingly. The induced magnetosphere shrinks, lowering the bow shock position. On the quasi-parallel shock side ($Y_{\mathrm{MSE}} < 0$ in Figure S1), the shock front becomes perturbed. The planetary ion plume plane is tilted because it must be perpendicular to the magnetic field direction. All these changes cause a change in regions where the solar wind loses its energy.

Crucially, the current distributions detailed above are not merely structural features; they are directly linked to planetary ion escape. Given that the current density is proportional to the ion flux for singly charged ions, the spatial and directional characteristics of these currents serve as a proxy for ion escape pathways. Specifically, the localized plume currents delineate the plume escape channel. Moreover, the cross-flow plume observed under quasi-parallel and parallel IMF orientations signifies the emergence of a distinct upstream escape route. By mapping these current-derived flux distributions, we identify the key regions where ions are transported away from Mars. This provides the physical foundation for the quantitative escape rate analysis presented in Section 3.2, where we integrate the relevant flux components across the boundaries of each identified escape channel.

3.2 Escape Rates under Various IMF Orientations

To investigate the IMF orientation dependence of the heavy ion escape rate, we quantify the tailward, plume, and upstream escape rates (defined in Section 2) for O^+, O_2^+, and CO_2^+ across the five IMF cases, as presented in Figure 3. For these cases, the IMF magnitude is held constant at ~5.6 nT, with the components specified as follows: perpendicular ([0, 5.59, 0] nT), Parker spiral IMF ([−3.13, 4.64, 0] nT), cone angle 30° ([−4.84, 2.80, 0] nT), cone angle 10° ([−5.51, 0.97, 0] nT), and parallel ([−5.58, 0.39, 0] nT).

Although O_2^+ constitutes the dominant escaping species, followed by O^+ and CO_2^+ because of production rate differences, the results show that all three species exhibit a similar response pattern to the IMF orientation. Specifically, the total escape rate follows a nonmonotonic trend: it decreases from the perpendicular to the cone angle 30° case, increases slightly from 30° to 10°, and then undergoes a dramatic surge from cone angle 10° to the parallel IMF case, with the highest escape rate. This nonmonotonic behavior results from the competition between ion escape from the tail and from the plume. As the cone angle decreases, the convective electric field weakens, causing the IMB to move closer to Mars. This shift allows solar wind energy to be transported more efficiently to the ionosphere, enhancing plume escape. In contrast, tail escape is influenced by the $\boldsymbol{J}\times\boldsymbol{B}$ force, which weakens as the induced magnetosphere becomes less developed and eventually degenerates under parallel IMF conditions, leading to a reduction in tail escape. The interplay between these two competing processes gives rise to the observed nonmonotonic trend. Consequently, the observed trend indicates that the induced magnetosphere switches to a degenerate state when the IMF cone angle drops below 10°, consistent with the framework of Zhang Q et al. (2024). In this state, the diminished magnetic barrier most effectively facilitates ion escape, thereby producing the maximum loss rates.

The relative contribution of different escape channels shifts dramatically with the IMF orientation. As the IMF rotates from perpendicular to parallel, the proportion of escape contributed by the tail escape gradually decreases, whereas that from the plume escape progressively increases and becomes predominant.

Notably, upstream escape exhibits a marked increase under the parallel IMF, whereas it is negligible from the perpendicular to cone angle 30° IMF. A similar substantial contribution from

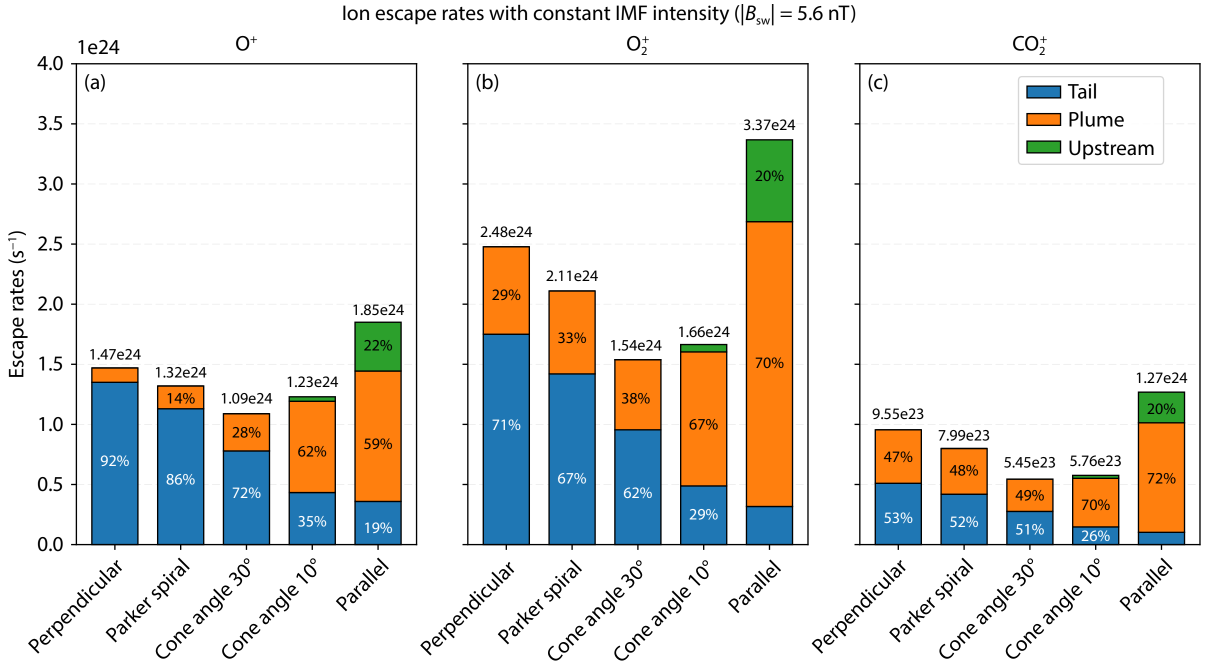

Figure 3. Ion escape rates of (a) O$^+$, (b) O$_2$$^+$, (c) CO$_2$$^+$ under IMF vectors of constant magnitude ($|B_{sw}|$ = ~5.6 nT) across various IMF orientations: perpendicular IMF ([0, 5.59, 0] nT); Parker spiral IMF ([−3.13, 4.64, 0] nT); cone angle 30° IMF ([−4.84, 2.80, 0] nT); cone angle 10° IMF ([−5.51, 0.97, 0] nT); parallel IMF ([−5.58, 0.39, 0] nT). For each ion species and IMF condition, the total escape rate is decomposed into three channels: tailward (blue), plume (orange), and upstream (green) ion escape.

upstream escape was reported in the study by Zhang Q et al. (2025), which identified the ambipolar electric field as a key driver for this upstream channel—a pathway absent in nominal cases. These results demonstrate that parallel IMF conditions drive a fundamental restructuring of ion escape pathways, where the enhancement in plume and upstream escape more than compensates for the reduction in tailward escape, thereby increasing the total ion escape rates.

4. Discussion

Figure 3 examines the dependence of ion escape on the IMF orientation by rotating the IMF vector under a constant magnetic field magnitude ($|B_{sw}|$ = ~5.6 nT). Our results show that for all heavy ion species (O$^+$, O$_2$$^+$, and CO$_2$$^+$), the escape rates at a parallel IMF are significantly higher than those at a perpendicular IMF, and the plume escape rate decreases monotonically as the cone angle increases. This trend is consistent with the findings of Zhang Q et al. (2023). Specifically, they reported that under high extreme ultraviolet radiation conditions, with the IMF magnitude ranging from 2.5 to 3.5 nT, the total escape rate and plume escape rate decrease as the cone angle increases. Additionally, they examined the effect of IMF magnitude and found that the total escape rate and plume escape rate decrease as the IMF magnitude increases. Furthermore, the later hybrid simulation study by Zhang Q et al. (2025) showed that under extremely small cone angles (4°) where the induced magnetosphere degenerates, the total heavy ion escape rate is nearly an order of magnitude higher than that in the nominal Parker spiral case (55°). This enhancement is accompanied by a greatly increased plume escape and the emergence of a unique upstream escape channel driven by the ambipolar electric field. However, an important distinction between the studies is that in Zhang Q et al. (2023, 2025), the simulation cases involved variations in multiple solar wind parameters (solar wind speed, magnetic field strength, density, proton temperature, etc.) and were tailored to specific observational events. In contrast, our study holds all other solar wind parameters constant, and these parameters are comparable to the low extreme ultraviolet radiation case examined by Zhang Q et al. (2023) under their specific simulation setup.

Furthermore, in this constant $|B_{sw}|$ series, the Alfvén Mach number remains constant at $M_A = 6.36$ (based on upstream V_{sw} = 350 km/s, $n = 4.9$ cm^{-3}), which is well within the super-Alfvénic regime typical of present-day Mars. This approach inherently alters the B_y component, thereby modulating the strength of the solar wind convective electric field ($|E_{sw}|$). Consequently, changes in geometric configuration (θ) are intrinsically coupled with changes in electric field strength, mixing their respective contributions to escape variability.

To decouple these two factors, we design a new simulation exercise (Figure 4), in which the B_y component is held constant (~5.6 nT) to ensure a constant $|E_{sw}|$. The cone angle is then varied by adjusting the B_x component. The simulated configurations include perpendicular IMF ([0, 5.59, 0] nT), Parker spiral IMF ([−3.75, 5.59, 0] nT), a 30° cone angle ([−9.69, 5.59, 0] nT), a 10° cone angle ([−31.73, 5.59, 0] nT), and parallel IMF ([−80.01, 5.59, 0] nT). Accompanying these variations is a fundamental shift in the flow regime, as indicated by the Alfvén Mach number (M_A): it declines from a super-Alfvénic value in the perpendicular case (M_A = 6.36), transitions to a marginal state at the 10° cone angle (M_A = 1.10), and becomes sub-

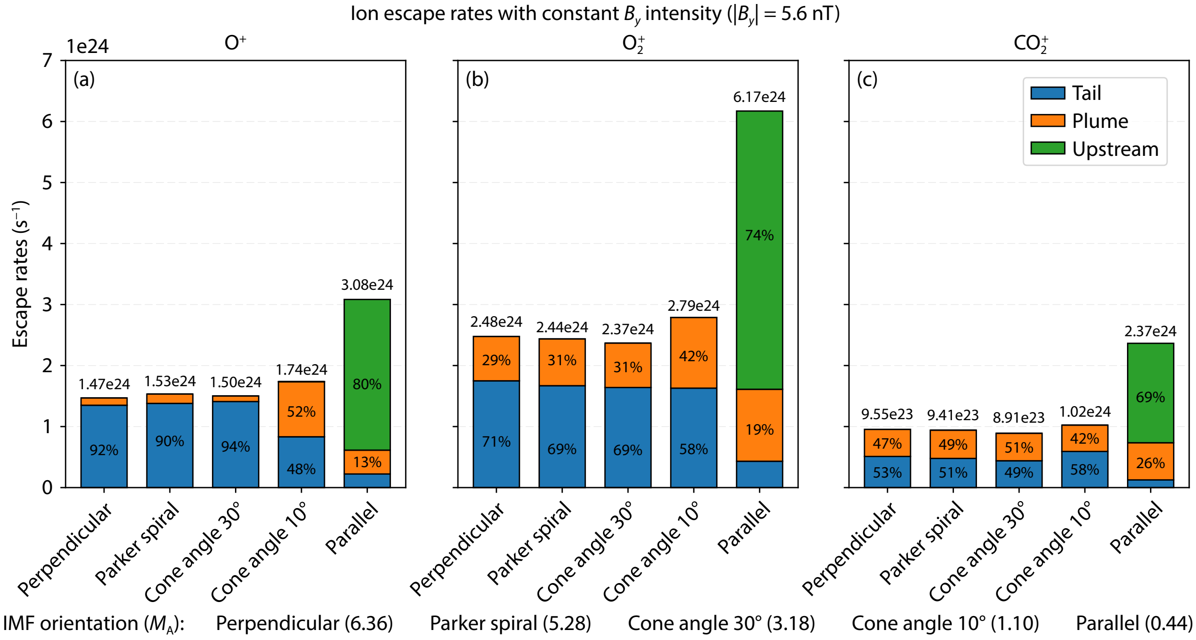

Figure 4. Ion escape rates of (a) O⁺, (b) O_2^+, (c) CO_2^+ under five IMF orientations with the B_y component fixed at ~5.6 nT: perpendicular IMF ([0, 5.59, 0] nT); Parker spiral IMF ([−3.75, 5.59, 0] nT); cone angle 30° IMF ([−9.69, 5.59, 0] nT); cone angle 10° IMF ([−31.73, 5.59, 0] nT); parallel IMF ([−80.01, 5.59, 0] nT). The total escape rate is decomposed into three channels: tailward (blue), plume (orange), and upstream (green) ion escape. The corresponding Alfvén Mach number (M_A) for each IMF orientation is indicated below the figure, showing a transition from super-Alfvénic to sub-Alfvénic as the cone angle decreases.

Alfvénic in the parallel IMF case ($M_A = 0.44$).

In the super-Alfvénic regime ($M_A > 3.18$ for cone angles ≥ 30° in this series), the ion escape rates remain constant as the IMF B_x component increases so that the IMF cone angle reduces from 90° to 30°, even for each individual species. This overall stability indicates that a sufficiently strong electric field sustains a well-developed induced magnetosphere, with shielding capability largely unaffected by the growing B_x component. Escape in this regime is dominated by tailward and plume flows, with no upstream loss, confirming the integrity of the dayside magnetic barrier. The spatial distributions of heavy ion and solar wind proton currents under these super-Alfvénic conditions (from perpendicular to 30° cone angle) closely resemble those shown in Figures 1 and 2, respectively, as further demonstrated by the B_y-constant series in the Supplementary Information (Figures S2 and S3). This indicates that the interaction remains within the regime relevant to present-day Mars. Liu K et al. (2009) studied the effects of the B_x component on O⁺ escape from Venus using a different hybrid code (Kallio and Janhunen, 2002). They compared escape rates under perpendicular and 36° cone angle IMF conditions across various solar wind densities and found that the ion escape rate in the 36° cone angle case was ~25% higher than that in the perpendicular case. Because their model implementation, simulation setup, planetary size, ionospheric species, and ionospheric productions are all different from this work, we cannot simply pinpoint the reason for the discrepancy. More comprehensive studies on the effects of individual solar wind parameters on the ion escape process from induced magnetospheres are needed to clarify this divergence.

At a cone angle of 10°, where the flow enters a trans-Alfvénic state (M_A = 1.10), the escape rates for all heavy ion species exhibit a noticeable increase. Specifically for O⁺, this enhancement is characterized by a reduction in tailward escape coupled with a significant surge in plume escape. As the IMF aligns further to the parallel direction, the interaction transitions into the sub-Alfvénic regime ($M_A = 0.44$). Under these conditions, the nature of ion loss changes fundamentally: substantial upstream escape emerges, rendering direct comparisons with the super-Alfvénic cases inappropriate because of the breakdown of the magnetic barrier. Correspondingly, for a cone angle of 10°, the proton current distributions deviate markedly from the typical morphology associated with the Martian bow shock, reflecting the onset of sub-Alfvénic interaction (Figure S3). For the parallel IMF case, the interaction becomes fully sub-Alfvénic. Although such sub-Alfvénic conditions are rare for Mars in the present-day solar wind, the specific sub-Alfvénic regime examined here is not representative of typical Martian space weather conditions and is therefore not the focus of this study. Nevertheless, this regime holds significant relevance for exoplanetary studies because many close-in exoplanets are expected to be located within sub-Alfvénic stellar winds (e.g., Vidotto et al., 2023; Peña-Moñino et al., 2024), making our results a valuable analogue for understanding atmospheric erosion under such extreme conditions.

5. Summary

In this study, we investigate the influence of the IMF orientation on ion current systems and heavy ion escape at Mars using a hybrid model. Two simulation series are conducted to isolate different physical effects. The first series maintains a constant $|B_{sw}|$ (hence constant Alfvén Mach number $M_A = 6.36$), representing the super-Alfvénic regime typical of present-day Mars, with a varying IMF cone angle, altering the strength of the convective electric field. The second series keeps a constant B_y component (hence constant $|E_{\rm sw}|$), where the cone angle is varied by changing the B_x component, causing $M_{\rm A}$ to decrease from super-Alfvénic to trans-Alfvénic and ultimately to sub-Alfvénic values as the IMF approaches a parallel orientation.

Under the super-Alfvénic conditions relevant to present-day Mars (constant $|B_{\rm sw}|$ series), several key features emerge as the IMF rotates from perpendicular to parallel. The spatial morphology of heavy ion plumes undergoes a significant evolution, forming a distinct cross-flow plume characterized by a progressive deflection of ion flow from the electric field plane toward the magnetic field plane. The plume deflection exhibits a clear mass dependence as the IMF approaches a parallel orientation. Lighter ions (O^+) extend closer from the ionosphere, whereas heavier ions (CO_2^+) travel farther on a larger gyroradius, acting as an asymmetric, additional obstacle to the solar wind in the $-Y_{\rm MSE}$ hemisphere. In response, the solar wind proton current develops pronounced asymmetries under a parallel IMF, becoming largely diffused in the $-Y_{\rm MSE}$ hemisphere where the IMF is parallel to the local bow shock normal while the bow shock persists in the $+Y_{\rm MSE}$ hemisphere where the IMF is perpendicular to the local bow shock normal. Consequently, the total heavy ion escape rates exhibit a nonmonotonic dependence on the IMF orientation, reaching a minimum at a cone angle of 30° before increasing toward parallel IMF. This trend is driven by a shift from tail-dominated to plume-dominated escape, accompanied by a substantial enhancement of an upstream escape channel in the parallel IMF case, although this channel does not become dominant.

The constant B_y series allows us to decouple the effects of IMF geometry from those of the convective electric field. Within the range from perpendicular to a 30° cone angle, where the system remains in the super-Alfvénic regime, heavy ion escape is largely insensitive to the growing B_x component, indicating that the magnetic barrier maintains its shielding efficiency under conditions representative of present-day Mars. However, as the cone angle decreases further to 10° and eventually to parallel IMF, the system transitions into trans-Alfvénic and fully sub-Alfvénic regimes ($M_{\rm A} \approx 0.44$), serving as an exoplanet analogue. In these extreme sub-Alfvénic cases, the upstream escape channel becomes the dominant pathway, representing a new escape regime that is fundamentally distinct from the super-Alfvénic conditions of present-day Mars.

Acknowledgments

This work was supported by the National Natural Science Foundation of China (Grant Nos. 42188101, 42025404, 42374193, and 42578012), the National Key R&D Program of China (Grant Nos. 2022YFF0503700 and 2022YFF0503900), the Natural Science Foundation of Hubei Province, China (Grant 2025AFA030), the Fengyun Application Pioneering Project (FY-APP), and the Tencent X-plorer prize. This work was also supported by a special scholarship provided through the Graduate Student Exchange Program at Wuhan University, China. The Amitis simulations were performed using computational resources provided by the High Performance Computing Center North (HPC2N), Umeå University, Sweden. These resources were partly sponsored by Kempestiftelserna (Grant Nos. JCSMK25-0057 and JCK22-0035).

References

Acuña, M. H., Connerney, J. E. P., Wasilewski, P., Lin, R. P., Anderson, K. A., Carlson, C. W., McFadden, J., Curtis, D. W., Mitchell, D., … Ness, N. F. (1998). Magnetic field and plasma observations at Mars: Initial results of the Mars global surveyor mission. *Science*, *279*(5357), 1676–1680. https://doi.org/10.1126/science.279.5357.1676

Barabash, S., Fedorov, A., Lundin, R., and Sauvaud, J. A. (2007). Martian atmospheric erosion rates. *Science*, *315*(5811), 501–503. https://doi.org/10.1126/science.1134358

Brain, D., Barabash, S., Boesswetter, A., Bougher, S., Brecht, S., Chanteur, G., Hurley, D., Dubinin, E., Fang, X., … Terada, N. (2010). A comparison of global models for the solar wind interaction with Mars. *Icarus*, *206*(1), 139–151. https://doi.org/10.1016/j.icarus.2009.06.030

Brain, D. A., Mitchell, D. L., and Halekas, J. S. (2006). The magnetic field draping direction at Mars from April 1999 through August 2004. *Icarus, 182*(2), 464–473. https://doi.org/10.1016/j.icarus.2005.09.023

Brain, D. A., Bagenal, F., Ma, Y. J., Nilsson, H., and Stenberg Wieser, G. (2016). Atmospheric escape from unmagnetized bodies. *J. Geophys. Res.: Planets*, *121*(12), 2364–2385. https://doi.org/10.1002/2016JE005162

Burgess, D., Lucek, E. A., Scholer, M., Bale, S. D., Balikhin, M. A., Balogh, A., Horbury, T. S., Krasnoselskikh, V. V., Kucharek, H., … Walker, S. N. (2005). Quasi-parallel shock structure and processes. *Space Sci. Rev.*, *118*(1–4), 205–222. https://doi.org/10.1007/s11214-005-3832-3

Chang, Q., Xu, X. J., Xu, Q., Wang, J., Xu, J. Y., Ye, Y. D., and Zhang, T. L. (2020). The demagnetization of the Venusian ionosphere under nearly flow-aligned interplanetary magnetic fields. *Astrophys. J.*, *900*(1), 63. https://doi.org/10.3847/1538-4357/aba62a

Connerney, J. E. P., Acuña, M. H., Wasilewski, P. J., Ness, N. F., Rème, H., Mazelle, C., Vignes, D., Lin, R. P., Mitchell, D. L., and Cloutier, P. A. (1999). Magnetic lineations in the ancient crust of Mars. *Science*, *284*(5415), 794–798. https://doi.org/10.1126/science.284.5415.794

Cui, J., Yelle, R. V., Zhao, L. L., Stone, S., Jiang, F. Y., Cao, Y. T., Yao, M. J., Koskinen, T. T., and Wei, Y. (2018). The impact of crustal magnetic fields on the thermal structure of the Martian upper atmosphere. *Astrophys. J. Lett.*, *853*(2), L33. https://doi.org/10.3847/2041-8213/aaa89a

Dong, Y., Fang, X., Brain, D. A., McFadden, J. P., Halekas, J. S., Connerney, J. E., Curry, S. M., Harada, Y., Luhmann, J. G., and Jakosky, B. M. (2015). Strong plume fluxes at Mars observed by MAVEN: An important planetary ion escape channel. *Geophys. Res. Lett.*, *42*(21), 8942–8950. https://doi.org/10.1002/2015GL065346

Dong, Y., Fang, X., Brain, D. A., McFadden, J. P., Halekas, J. S., Connerney, J. E. P., Eparvier, F., Andersson, L., Mitchell, D., and Jakosky, B. M. (2017). Seasonal variability of Martian ion escape through the plume and tail from MAVEN observations. *J. Geophys. Res.: Space Phys.*, *122*(4), 4009–4022. https://doi.org/10.1002/2016JA023517

Du, H. L., Cao, X., Ni, B. B., Fu, S., Ma, X., Yun, X. T., Long, M. Y., and Luo, Q. (2022). Distribution of O^+ and O_2^+ fluxes and their escape rates in the near-Mars magnetotail: A survey of MAVEN observations. *Earth Planet. Phys.*, *6*(6), 536–545. https://doi.org/10.26464/epp2023002

Du, J., Zhang, T. L., Wang, C., Volwerk, M., Delva, M., and Baumjohann, W. (2009). Magnetosheath fluctuations at Venus for two extreme orientations of the interplanetary magnetic field. *Geophys. Res. Lett.*, *36*(9), L09102. https://doi.org/10.1029/2009gl037725

Fang, X. H., Ma, Y. J., Luhmann, J., Dong, Y. X., Brain, D., Hurley, D., Dong, C. F., Lee, C. O., and Jakosky, B. (2018). The morphology of the solar wind magnetic field draping on the dayside of Mars and its variability. *Geophys. Res. Lett.*, *45*(8), 3356–3365. https://doi.org/10.1002/2018gl077230

Fatemi, S., Poppe, A. R., Delory, G. T., and Farrell, W. M. (2017). AMITIS: A 3D GPU-based hybrid-PIC model for space and plasma physics. *J. Phys.: Conf. Ser.*, *837*, 012017. https://doi.org/10.1088/1742-6596/837/1/012017

Fowler, C. M., Hanley, K. G., McFadden, J., Halekas, J., Schwartz, S. J., Mazelle, C., Chaffin, M., Mitchell, D., Espley, J., … Curry, S. (2022). A MAVEN case study of radial IMF at Mars: Impacts on the dayside ionosphere. *J. Geophys. Res.: Space Phys.*, *127*(12), e2022JA030726. https://doi.org/10.1029/2022JA030726

Ganushkina, N. Y., Liemohn, M. W., and Dubyagin, S. (2018). Current systems in the Earth's magnetosphere. *Rev. Geophys.*, *56*(2), 309–332. https://doi.org/10.1002/2017RG000590

Garnier, P., Jacquey, C., Gendre, X., Génot, V., Mazelle, C., Fang, X., Gruesbeck, J. R., Sánchez‐Cano, B., and Halekas, J. S. (2022). The drivers of the Martian bow shock location: A statistical analysis of Mars Atmosphere and Volatile EvolutioN and Mars Express observations. *J. Geophys. Res.: Space Phys.*, *127*(5), e2021JA030147. https://doi.org/10.1029/2021JA030147

Jakosky, B. M., and Phillips, R. J. (2001). Mars' volatile and climate history. *Nature*, *412*(6843), 237–244. https://doi.org/10.1038/35084184

Jakosky, B. M., Grebowsky, J. M., Luhmann, J. G., Connerney, J., Eparvier, F., Ergun, R., Halekas, J., Larson, D., Mahaffy, P., … Yelle, R. (2015). MAVEN observations of the response of Mars to an interplanetary coronal mass ejection. *Science*, *350*(6261), aad0210. https://doi.org/10.1126/science.aad0210

Kallio, E., and Janhunen, P. (2002). Ion escape from Mars in a quasi-neutral hybrid model. *J. Geophys. Res.: Space Phys.*, *107*(A3), 1035. https://doi.org/10.1029/2001JA000090

Le, G., Russell, C. T. and Takahashi, K. (2004). Morphology of the ring current derived from magnetic field observations. *Ann. Geophys.*, *22*(4), 1267–1295. https://doi.org/10.5194/angeo-22-1267-2004

Li, S. B., Lu, H. Y., Cui, J., Yu, Y. Q., Mazelle, C., Li, Y., and Cao, J. B. (2020). Effects of a dipole-like crustal field on solar wind interaction with Mars. *Earth Planet. Phys.*, *4*(1), 23–31. https://doi.org/10.26464/epp2020005

Li, S. B., Lu, H. Y., Cao, J. B., Cui, J., Ge, Y. S., Zhang, X. X., Rong, Z. J., Li, G. K., Li, Y., … Wang, J. X. (2023). Global electric fields at Mars inferred from multifluid Hall-MHD simulations. *Astrophys. J.*, *949*(2), 88. https://doi.org/10.3847/1538-4357/acc842

Li, X. Z., Rong, Z. J., Gao, J. W., Wei, Y., Shi, Z., Yu, T., and Wan, W. X. (2020). A local Martian crustal field model: Targeting the candidate landing site of the 2020 Chinese Mars Rover. *Earth Planet. Phys.*, *4*(4), 420–428. https://doi.org/10.26464/epp2020045

Liu, K., Kallio, E., Jarvinen, R., Lammer, H., Lichtenegger, H. I. M., Kulikov, Y. N., Terada, N., Zhang, T. L., and Janhunen, P. (2009). Hybrid simulations of the O^+ ion escape from Venus: Influence of the solar wind density and the IMF x component. *Adv. Space Res.*, *43*(9), 1436–1441. https://doi.org/10.1016/j.asr.2009.01.005

Lundin, R., Barabash, S., Fedorov, A., Holmström, M., Nilsson, H., Sauvaud, J. A., and Yamauchi, M. (2008). Solar forcing and planetary ion escape from Mars. *Geophys. Res. Lett.*, *35*(9), L09203. https://doi.org/10.1029/2007GL032884

Lundin, R., Barabash, S., Dubinin, E., Winningham, D., and Yamauchi, M. (2011). Low-altitude acceleration of ionospheric ions at Mars. *Geophys. Res. Lett.*, *38*(8), L08108. https://doi.org/10.1029/2011GL047064

Peña-Moñino, L., Pérez-Torres, M., Varela, J., and Zarka, P. (2024). Magnetohydrodynamic simulations of the space weather in Proxima b: Habitability conditions and radio emission. *A&A*, *688*, A138. https://doi.org/10.1051/0004-6361/202349042

Phillips, J. L., Luhmann, J. G., and Russell, C. T. (1986). Magnetic configuration of the Venus magnetosheath. *J. Geophys. Res.: Space Phys.*, *91*(A7), 7931–7938. https://doi.org/10.1029/ja091ia07p07931

Ramstad, R., Brain, D. A., Dong, Y. X., Espley, J., Halekas, J., and Jakosky, B. (2020). The global current systems of the Martian induced magnetosphere. *Nat. Astron.*, *4*(10), 979–985. https://doi.org/10.1038/s41550-020-1099-y

Shi, Z., Rong, Z. J., Fatemi, S., Slavin, J. A., Klinger, L., Dong, C., Wang, L., Zhong, J., Raines, J. M., … Wei, Y. (2022). An eastward current encircling Mercury. *Geophys. Res. Lett.*, *49*(10), e2022GL098415. https://doi.org/10.1029/2022GL098415

Song, Y. H., Li, Y., Lu, H. Y., Cao, J. B., and Li, S. B. (2025). The impact of interplanetary magnetic field intensity on the Martian ionosphere. *A&A*, *694*, A189. https://doi.org/10.1051/0004-6361/202453085

Trotignon, J. G., Mazelle, C., Bertucci, C., and Acuña, M. H. (2006). Martian shock and magnetic pile-up boundary positions and shapes determined from the Phobos 2 and Mars Global Surveyor data sets. *Planet. Space Sci.*, *54*(4), 357–369. https://doi.org/10.1016/j.pss.2006.01.003

Vidotto, A. A., Bourrier, V., Fares, R., Bellotti, S., Donati, J. F., Petit, P., Hussain, G. A. J., and Morin, J. (2023). The space weather around the exoplanet GJ 436b: II. Stellar wind–exoplanet interactions. *A&A*, *678*, A152. https://doi.org/10.1051/0004-6361/202347237

Wang, X. D., Fatemi, S., Nilsson, H., Futaana, Y., Holmström, M., and Barabash, S. (2023). Solar wind interaction with Mars: Electric field morphology and source terms. *Mon. Not. Roy. Astron. Soc.*, *521*(3), 3597–3607. https://doi.org/10.1093/mnras/stad247

Wang, X. D., Fatemi, S., Holmström, M., Nilsson, H., Futaana, Y., and Barabash, S. (2024). Martian global current systems and related solar wind energy transfer: hybrid simulation under nominal conditions. *Mon. Not. Roy. Astron. Soc.*, *527*(4), 12232–12242. https://doi.org/10.1093/mnras/stad3486

Zhang, C., Dong, C. F., Zhou, H. Y., Halekas, J., Li, X. M., Gao, J. W., Shen, H. W., Wang, X. D., Nilsson, H., ... Mitchell, D. L. (2025). Global energy transport and conversion in the solar wind-Mars interaction: MAVEN observations. *J. Geophys. Res.: Planets*, *130*(10), e2025JE009295. https://doi.org/10.1029/2025JE009295

Zhang, Q., Holmström, M., Wang, X. D., Nilsson, H., and Barabash, S. (2023). The influence of solar irradiation and solar wind conditions on heavy ion escape from Mars. *J. Geophys. Res.: Space Phys.*, *128*(10), e2023JA031828. https://doi.org/10.1029/2023JA031828

Zhang, Q., Barabash, S., Holmstrom, M., Wang, X. D., Futaana, Y., Fowler, C. M., Ramstad, R., and Nilsson, H. (2024). Mars's induced magnetosphere can degenerate. *Nature*, *634*(8032), 45–47. https://doi.org/10.1038/s41586-024-07959-z

Zhang, Q., Barabash, S., Holmström, M., Wang, X. D., Futaana, Y., Fowler, C. M., Ramstad, R., and Nilsson, H. (2025). Ion escape from degenerate induced magnetospheres: The case of Mars. *Geophys. Res. Lett.*, *52*(12), e2025GL116161. https://doi.org/10.1029/2025GL116161

Zhang, T. L., Du, J., Ma, Y. J., Lammer, H., Baumjohann, W., Wang, C., and Russell, C. T. (2009). Disappearing induced magnetosphere at Venus: Implications for close-in exoplanets. *Geophys. Res. Lett.*, *36*(20), L20203. https://doi.org/10.1029/2009GL040515